Comparison of different Quantitative Susceptibility Mapping (QSM) algorithms in brain tissue

Sophia Schmidt, Stephanie Mangesius, Elke R. Gizewski, Daniel Sieber, and Christoph Birkl

***Abstract*—Quantitative susceptibility mapping (QSM) is a novel post-processing technique that computes the underlying susceptibility distribution from MRI phase data. Strong susceptibility shifts introduce streaking artifacts in the reconstructed map that remain challenging to reduce. In this study, magnitude and phase data were acquired from the brain of one healthy and one glioblastoma patient using a multi-echo gradient-recalled echo (GRE) sequence. Several investigations were conducted, including the performance evaluation of three different algorithms, namely MEDI, RTS, and STAR-QSM, the comparison between echo-time (TE)-dependent and multi-echo QSM, and the separate calculation of healthy and tumor-affected brain tissue with subsequent merging. Visual inspections and data analysis with MATLAB showed that the different algorithms performed well in healthy brain conditions, but introduced artifacts when reconstructing large dynamic ranges in susceptibilities. The combination of multi-echo QSM together with excluding the glioblastoma region during reconstruction resulted in high-quality susceptibility maps. Subsequent superposition of the missing tumor region composed of a full-brain susceptibility map with reduced artifacts, offering promising advancements in QSM accuracy for pathological brain conditions.**

***Index Terms*—Quantitative Susceptibility Mapping, Glioblastoma, Masking, TE-dependent QSM, Mulit-echo QSM, Superposed, Artifact Reduction.**

I. Introduction

Scientists have developed a post-processing technique, known as Quantitative Susceptibility Mapping (QSM), to extract information about the magnetic susceptibility distribution in biological objects or samples using MRI phase measurements [1]. By quantifying the magnetic susceptibility properties of tissues, QSM offers a possibility to non-invasively assess changes in the brain with improved quality and contrast. Therefore, enhancing diagnostic specificity, treatment planning, and monitoring treatment response in glioblastoma patients, for example. Deistung et al. [2] showed that QSM can be used to quantitatively differentiate between paramagnetic blood deposits and diamagnetic calcifications within a glioblastoma. The authors state, that the presence of diamagnetic calcifications may represent an important biomarker for guiding therapy decisions and evaluating treatment responses and outcomes. Making it a valuable tool for differentiating and assessing the grade of brain tumors. Zeng et al. [3] found a significant correlation between glioma grading and morphological changes in QSM and stated that QSM has promising potential in evaluating gliomas. Furthermore, according to the findings of Reith et al. [4], a potential biomarker for tumor severity grading was identified by means of differences in iron content in the basal ganglia, accessible only with QSM.

However, QSM is not yet adapted in clinical settings due to the lack of precise and reliable reconstruction algorithms that produce sufficient artifact-free susceptibility maps. Particularly in pathological conditions with strong susceptibility shifts, huge streaking artifacts occur that remain challenging to reduce. Additionally, physicians and radiologists are not adequately familiar with the new contrast of the resulting images, which hinders a meaningful interpretation.

Motivated by the emerging research field of QSM, this paper aims to conduct several investigations, both in a healthy brain subject and in a patient subject suffering from glioblastoma. To find an algorithm that is closest to artifact-free susceptibility reconstruction, different open-source QSM algorithms were used that participated in the "2016 Reconstruction Challenge" [5], namely MEDI, RTS, and STAR-QSM. In the healthy subject, it is first investigated how susceptibility values temporally change over the echo time in defined regions of interest (ROI) with a subsequent evaluation of the performance of the used algorithms. For the tumor patient, the performance of the different algorithms is tested as well with changing various brain masks as input. Thereafter, susceptibility maps reconstructed at single echo times (TE-dependent QSM) are compared with multi-echo QSM results. Finally, with the overall best results from the previous evaluation, a separate QSM calculation of the healthy and tumor-affected brain region is performed with a subsequent merging of both results, composing a superposed whole-brain susceptibility map.

II. Methods

In this study, several investigations for both a healthy patient (H) and a glioblastoma patient (G) were conducted, which are listed below. These statements are examined using the methods explained in the following sections. With this approach, differences between applying QSM algorithms, namely MEDI, RTS, and STAR-QSM, to a healthy and a pathological condition were studied.

- H 1 TE-dependent QSM investigating the influence of echo time on susceptibility values
- H 2 General QSM performance of the different algorithms by analyzing various quantitative error metrics
- G 3 Algorithm performance using different input masks in TE-dependent QSM
- G 4 Comparison of multi-echo QSM and TE-dependent QSM
- G 5 Separate QSM calculation of healthy and tumor-affected brain tissue with subsequent merging

S. Schmidt and D. Sieber are with the Department of Medical and Health Technologies, MCI, Innsbruck, Austria

S. Mangesius, E. Gizewski and C. Birkl are with the Department of Neuroradiology, Medical University, Innsbruck, Austria

A. Datasets

Fully anonymized datasets of one healthy and one glioblastoma patient were provided by the Department of Neuroradiology, Medical University in Innsbruck. The study was approved by the local Ethics Committee (EK 1226/2020). Magnitude and phase images for both datasets with whole-brain coverage were acquired on a 3 Tesla (T) Siemens Skyra scanner using a 3D spoiled GRE sequence and adaptive combine algorithm for coil combination with the following parameters: Echo time (TE) = $4.92 : 4.92 : 29.51\,\mathrm{ms}$, repetition time (TR) = $35.0\,\mathrm{ms}$, flip angle (FA) = $15°$, bandwidth (BW) = $240\,\mathrm{Hz/pixel}$, matrix size = 180x224x144. The total acquisition time was $5{:}04\,\mathrm{min}$ for both subjects.
Additionally, T1-weighted images with a T1 MPRAGE sequence were acquired on the same scanner with the following parameters: inversion time (TI) = $1.1\,\mathrm{ms}$, TE = $0.3\,\mathrm{ms}$, TR = $2.11\,\mathrm{ms}$, FA = $8°$, BW = $250\,\mathrm{Hz/pixel}$, matrix size = 180x224x144. The total acquisition time was $3{:}37\,\mathrm{min}$.

B. Mask generation

Individual binary masks were created using FMRIB Software Library (FSL) [6] and Insight Toolkit (ITK)-SNAP [7], which were later applied to the different algorithms. In the healthy dataset, the brain mask was generated using FSL brain extraction tool (BET) [6] (threshold = 0.5) from the GRE magnitude image of the last echo. For the glioblastoma patient, brain masks were created for each individual echo ($TE_1 - TE_6$) of the GRE sequence from their corresponding magnitude images. The masks became smaller as the echo time increased due to signal dropout around regions with high gradients [8], such as brain or tumor boundaries. Consequently, the tumor region is excluded in the last echo (TE_6). Additionally, a T1 mask was generated for the glioblastoma patient using BET on the T1-weighted magnitude image acquired in a separate scan. To align the T1 mask with the GRE sequence, linear registration with FSL FLIRT was performed.
To estimate QSM only for the tumor-affected brain region, an inverse tumor mask was generated based on the E6 mask. The mask was dilated using FSL Maths. Figure 1 demonstrates an adapted processing scheme in order to investigate a separate QSM calculation on the healthy and tumor-affected brain region with subsequent merging (Statement G 5).

C. Algorithms

QSM was performed in MATLAB (The MathWorks, Inc. Natick MA, USA) using three open-source algorithms:

1) MEDI is incorporated in the MEDI toolbox from the Cornell MRI research lab (http://pre.weill.cornell.edu/mri/pages/qsm.html)
2) RTS is available from Christian Kames' GitHub repository (https://github.com/kamesy/QSM.m)
3) STAR-QSM is embedded in the STI Suite toolbox from Hongjiang Wei and Chunlei Liu from the University of California, Berkeley, USA (https://people.eecs.berkeley.edu/~chunlei.liu/software.html)

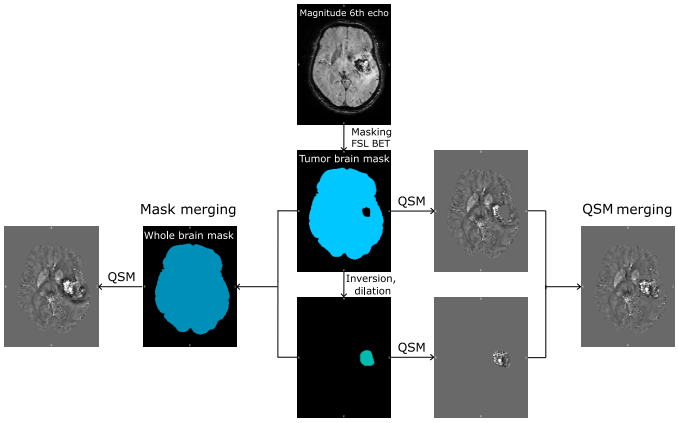

Fig. 1: Illustration of the QSM processing scheme to investigate Statement G 5. A tumor brain mask was generated using FSL BET from the sixth echo magnitude image. By inverting the brain mask, the tumor mask was created and dilated. On the left side, both masks were merged, resulting in a whole brain mask, before performing QSM. On the right side, QSM was calculated on both masks individually with subsequent merging of the resulting susceptibility maps.

Each algorithm employs individual methods for the post-processing steps that are summarized in Table I. These include phase unwrapping to eliminate aliasing from the wrapped phase, background field removal to separate the background from the local field, and dipole inversion to solve the inverse problem from field perturbation to magnetic susceptibility [9]. The reconstructed susceptibility maps were stored separately and further evaluated using ITK-SNAP and MATLAB for visual and statistical analysis, respectively.

TABLE I: Comparison of the methods in the used algorithms.

	MEDI	RTS	STAR-QSM
Phase unwrapping	Region growing algorithm	Laplacian phase unwrapping	Laplacian phase unwrapping
Background field removal	PDF	V-SHARP	V-SHARP
Dipole inversion (DI)	Morphology Enabled DI	Rapid Two-Step DI	Streaking Artifact Reduction

D. QSM data analysis

To investigate changing regional susceptibility values (Statement H 1), six regions of interest (ROI) were defined. For that, the T1 weighted magnitude image of the healthy subject was registered to the GRE sequence with FSL FLIRT. To generate the individual segments, FSL FIRST, an automated segmentation tool, was then applied and afterward binarized in a custom MATLAB script. Figure 2 shows the corresponding segments, namely caudate, putamen, and pallidum from an axial, coronal, sagittal, and 3D volume view.
To evaluate algorithm performance (Statements H 2 and G 3), the quantitative error metrics from the "2016 Reconstruction Challenge" [5] were adapted in MATLAB. Because of the lack of a gold-standard ground truth, MEDI and RTS were compared to the STAR-QSM algorithm as a reference. The error metrics include:

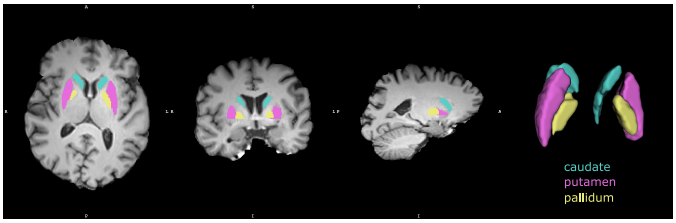

Fig. 2: Illustration of the six defined regions of interest from different views. From left to right: axial, coronal, sagittal, and 3D volume.

- The root mean squared error (RMSE) measures the average difference between pixel values of the reconstructed QSM image and the ground truth image [5]. A lower RMSE indicates a closer match to the reference image.
- The high-frequency error norm (HFEN) quantifies deviations at high spatial frequencies. It involves applying a Laplacian of a Gaussian (LoG) filter to both the reference and input volumes, then calculating the L2 norm of the difference and normalizing it by the LoG-filtered reference [10]. Smaller values indicate better performance.
- The structural similarity index (SSIM) aims to better represent the visual similarity between the image under consideration and the reference image [11]. It is normalized between 0 and 1, with 1 being the best possible result.

III. Results

A. TE-dependent QSM on the healthy dataset (H1)

A single axial slice from the resulting susceptibility maps of the healthy dataset is shown in Figure 3. TE-dependent QSM is performed on the phase images at each echo time ($TE_1 - TE_6$) using the MEDI, RTS, and STAR-QSM algorithms, from the first to the third row respectively. For MEDI and RTS, the susceptibility maps are scaled from -1 to $1\,ppm$, due to a greater variation in susceptibility values, and for STAR-QSM from -0.15 to $0.15\,ppm$, indicated by the color bar on the right side. Upon visual inspection, the results are similar across the algorithms, with increased contrast observed in higher echoes. However, the results of RTS appear overly smoothed.

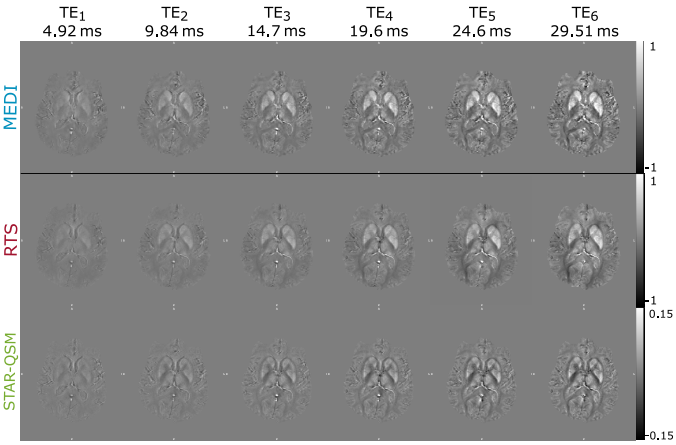

Fig. 3: Reconstructed susceptibility maps from the different algorithms at each echo time on the healthy dataset. Susceptibility values for MEDI and RTS are scaled from -1 to $1\,ppm$, and for the STAR-QSM from -0.15 to $0.15\,ppm$.

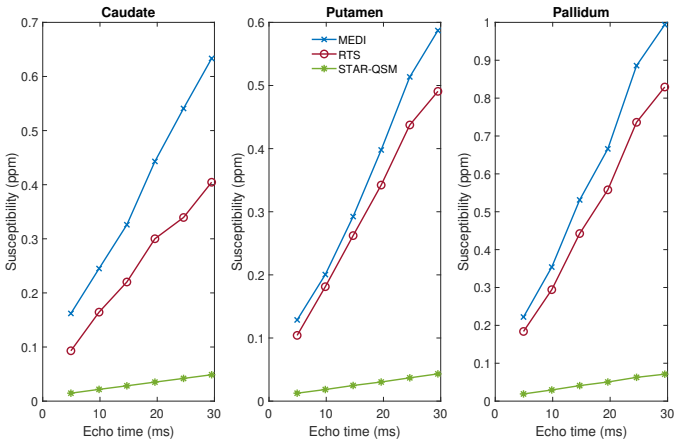

Fig. 4: Changes of mean susceptibility values over echo times in the defined regions of interest caudate (left), putamen (middle), and pallidum (right) for the three different algorithms.

The mean susceptibility values from the resulting quantitative susceptibility maps in the defined ROI from Section II-D were calculated and plotted in MATLAB (see Figure 4). This evaluation demonstrates that the susceptibility values in each ROI increase with the echo time for each algorithm, correlating to the visual findings from above. Compared to a slight overall increase in susceptibility values for the STAR-QSM algorithm, the gain in susceptibility for the other two algorithms is much higher. Table II summarizes the mean susceptibility values and standard deviation in the third echo ($TE_3 = 14.7\,ms$). It shows that MEDI and RTS have susceptibility values that are 10 times higher than STAR-QSM.

TABLE II: Mean susceptibility value and standard deviation at $TE_3 = 14.7\,ms$ in the ROI for MEDI, RTS and STAR-QSM.

	Caudate χ ($ppm \pm ppm$)	Putamen χ ($ppm \pm ppm$)	Pallidum χ ($ppm \pm ppm$)
MEDI	0.3260 ± 0.1181	0.2924 ± 0.1503	0.5312 ± 0.1595
RTS	0.2202 ± 0.0829	0.2622 ± 0.1384	0.4425 ± 0.1258
STAR-QSM	0.0283 ± 0.0117	0.0248 ± 0.0223	0.0410 ± 0.0207

B. General performance of algorithms on the healthy dataset (H2)

In order to compare the performance of MEDI and RTS to the reference algorithm (STAR-QSM), a metrics analysis was conducted as described in Section II using MATLAB. Figure 5 displays the different metrics in each subplot. It can be observed that RTS outperformed MEDI in terms of RMSE and HFEN, indicating greater agreement with the reference values of the third algorithm. Conversely, MEDI was found to be more structurally similar to STAR-QSM than RTS, indicated by the SSIM. Both algorithms exhibited high fluctuations in the first echoes, with the last echo of RTS displaying the most dissimilar result compared to the reference image. In general, lower echo times indicated a higher level of agreement compared to higher echo times across all three metrics, except for the second echo in the SSIM.

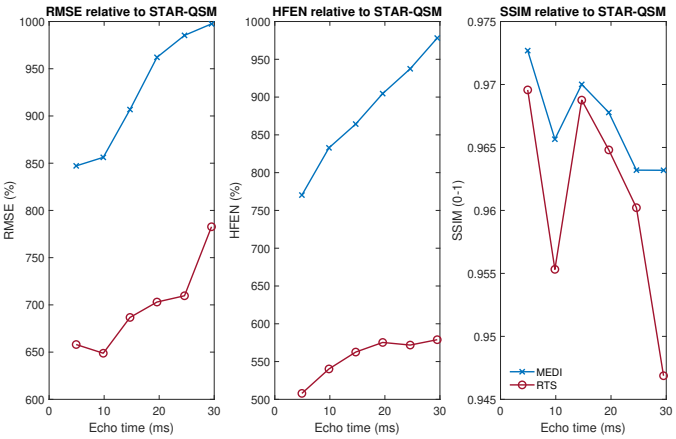

Fig. 5: Metric evaluation of MEDI and RTS relative to STAR-QSM on the healthy dataset. From left to right: RMSE, HFEN and SSIM.

C. *Algorithm performance using different input masks on the glioblastoma dataset (G3)*

For the TE-dependent QSM calculation on the patient dataset, the different masks were utilized to investigate the performance for all three algorithms in each case.

Figure 6 shows the reconstructed susceptibility maps at the same single axial slice, with the individual masks, E6 mask, and T1 mask applied, respectively. To enhance the comparability of the occurring artifacts and reconstruction accuracy, the susceptibility values were scaled from the local minimum to the local maximum of each map.

In Figure 6a the individual masks were applied, resulting in a hole in the last echo of the reconstructed map. Although the tumor region is excluded in the last echo, high susceptibility shifts around the tumor outline are visible. Furthermore, each algorithm erodes the input mask differently, affecting brain delineation and tumor hole size. Visually compared, the reconstructed maps are relatively similar to each other. The RTS algorithm exhibits shadowing artifacts in the posterior part of the brain, which increase with the echo time. Ring-shaped artifacts also appear around the tumor region, and the maps appear smoothed compared to other algorithms, lacking structural details in white and gray matter.

When applying the E6 mask (Figure 6b) similar effects appear as with the individual masks. However, RTS and STAR-QSM show fewer artifacts induced by the tumor region than in the evaluation before. More structural details can be seen, especially in lower echoes. In general, all algorithms perform slightly better when the E6 mask is applied. Nevertheless, susceptibility information in the glioblastoma region are missing.

Using the T1 mask (Figure 6c) results in comparable susceptibility maps for MEDI and STAR-QSM. However, the STAR-QSM algorithm exhibits more pronounced ring-shaped artifacts around the tumor area, which are not prominent when using the E6 mask. RTS shows noticeable streaking artifacts that are more prominent in higher echo times, especially in the frontal lobe area, significantly affecting QSM quality.

A metric analysis of the influence of the individual masks, E6 mask, and T1 mask on the susceptibility maps in each echo was performed in MATLAB. The evaluation is displayed in Figure 7 representing the RMSE, HFEN, and SSIM of MEDI and RTS relative to STAR-QSM. Shades of blue depict the performance of MEDI, and shades of red the performance of RTS. It is noteworthy that the metric evaluation of the healthy

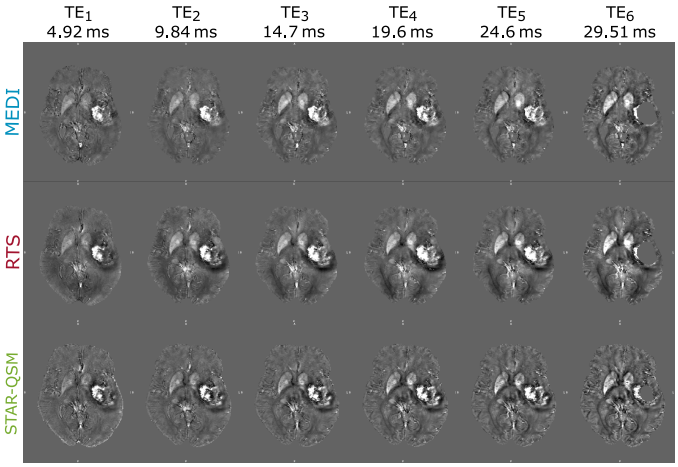

(a) Susceptibility maps from the different algorithms at each echo with the **individual masks** applied.

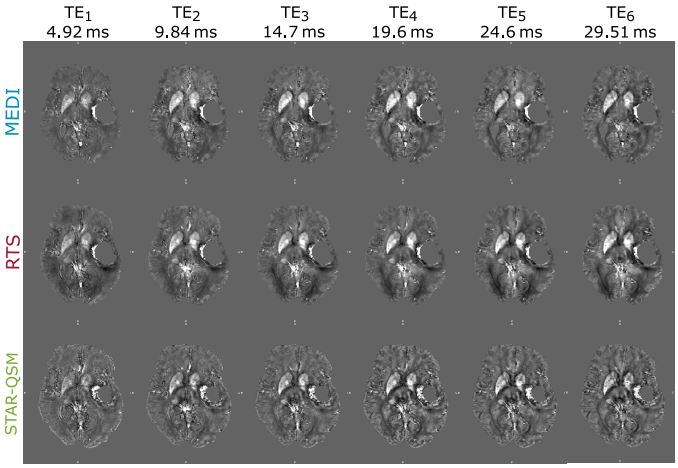

(b) Susceptibility maps from the different algorithms at each echo with the **E6 mask** applied.

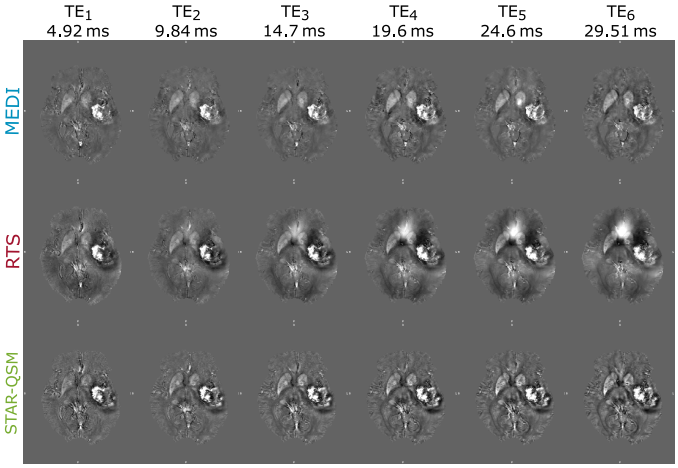

(c) Susceptibility maps from the different algorithms at each echo with the **T1 mask** applied.

Fig. 6: Reconstructed susceptibility maps of the different algorithms with the (a) individual masks (b) E6 mask and (c) T1 mask applied. In each case, the susceptibility values are scaled from the minimum to the maximum of the respective map.

and the tumor patient correlates in a way that RTS outperforms MEDI for RMSE and HFEN, but the opposite is observed for SSIM. For the glioblastoma patient, the metric evaluation reflects the visual findings from above. RTS and MEDI algorithms show similar evaluations for individual masks and the E6 mask, with minor deviations. Both masks share the same metric values in the last echo since the masks are equal. However, the T1 mask exhibits worse performance compared to other masks in RMSE, HFEN, and SSIM evaluations. Although not evident in visual evaluation, the plot indicates that the T1 mask also performs worse in MEDI for the first two metrics compared to other masks. However, no significant rash of the T1 mask is seen with SSIM.

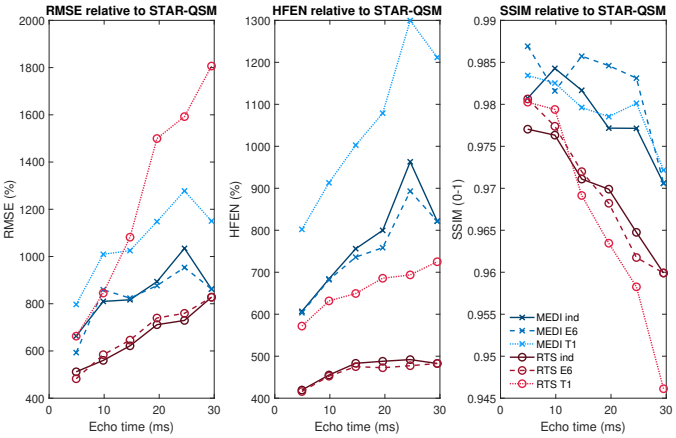

Fig. 7: Metrics evaluation of MEDI (shades of blue) and RTS (shades of red) relative to STAR-QSM on the tumor patient dataset. Straight, dashed and dotted lines represent the individual, E6, and T1 masks, respectively. From left to right: RMSE, HFEN and SSIM.

D. Comparison multi-echo QSM and TE-dependent QSM (G4)

The comparison between multi-echo QSM and TE-dependent QSM was conducted for MEDI and STAR-QSM since the RTS MATLAB script lacks of a combination of magnitude or phase images. Figure 8 displays the results with the E6 and T1 masks applied to MEDI and STAR-QSM in the first row, followed by TE-dependent results in the second row. TE-depenendet susceptibility maps were selected that showed most similar susceptibility ranges as the results of multi-echo QSM. In order to compare the different results within an applied algorithm, the susceptibility values for MEDI results were scaled from - 0.3 to $0.4\,ppm$ and from - 0.03 to $0.05\,ppm$ for STAR-QSM. Therefore, MEDI reconstructed susceptibility values that are 10 times higher than the ones from STAR-QSM.

From a visual perspective, MEDI produces artifacts of low susceptibility values in the anterior part and high susceptibility values in the posterior part of the brain when performing multi-echo QSM. The results appear overly smooth compared to TE-dependent QSM. For STAR-QSM, the multi-echo QSM image with the E6 mask used results in an almost artifact-free susceptibility map. Similar results can be obtained with the TE-dependent first echo image, but with less contrast between gray and white matter. Only the high susceptibility shifts in the remaining tumor region, which were not properly masked, cause halo artifacts in the vicinity of this region. However, when using the T1 mask, shadow artifacts around the tumor region are more evident in both multi-echo and TE-dependent QSM.

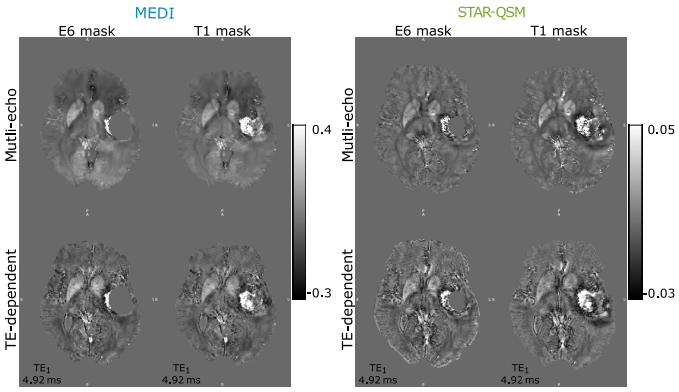

Fig. 8: Reconstructed QSM images from MEDI and STAR-QSM at the same axial slice. Comparing multi-echo QSM (first row) and TE-dependent QSM (second row) using the E6 and T1 mask.

E. Separate QSM calculation of healthy and tumor-affected brain tissue with subsequent merging (G5)

Figure 9 shows the comparison of the adapted processing scheme presented in Figure 1. The effect of a separate QSM calculation of healthy and tumor-affected brain tissue, with subsequent merging of the individual results (QSM merging) is compared to a regular QSM reconstruction using a whole-brain mask (mask merging). To ensure comparability, all maps were scaled from - 0.03 to $0.05\,ppm$.

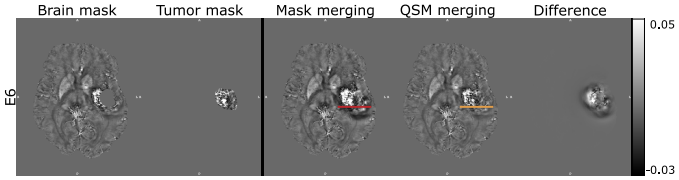

Fig. 9: Reconstructed susceptibility maps in one axial slice by applying the E6 brain mask and its inverse E6 tumor mask. Comparing the influence of whole brain QSM calculation (mask merging) and separate healthy and tumor-affected brain tissue calculation with subsequent merging (QSM merging). The difference image is shown on the right.

From a visual perspective, it can be seen that QSM merging results in a less artifact-prone susceptibility map compared to the mask merging method. While shadowing artifacts appear in the mask merging result, they are less prominent using QSM merging. The difference image demonstrates, that applying the two methods does not affect the healthy brain tissue, but deviations around the tumor region are apparent.

Figure 10 displays straight-line profiles of susceptibilities across the tumor region (from right to left in radiological conversion) for the two different methods. The maps differ most outside the tumor region, with mask merging (red line) showing higher negative susceptibility values correlating to halos around the tumor compared to QSM merging (orange line). Intratumoral variations are present in both methods but

QSM merging shows fewer fluctuations compared to mask merging.

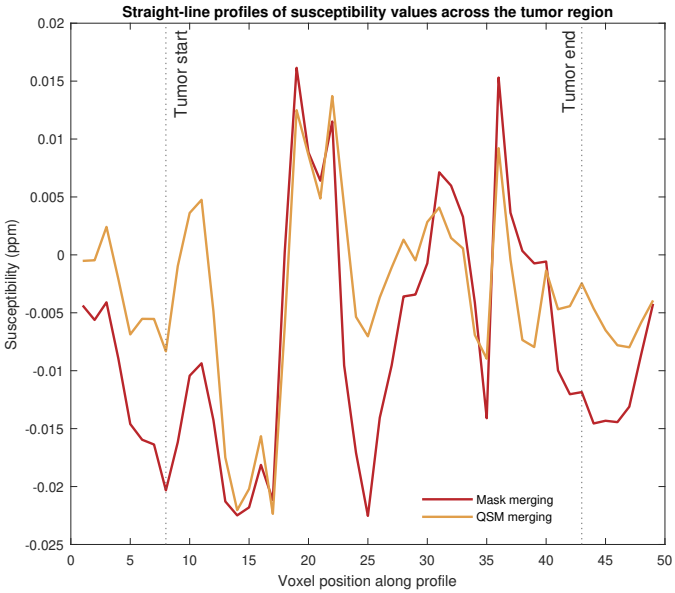

Fig. 10: Straight-line profiles of susceptibility values across the tumor: Mask merging (red), and QSM merging (orange).

IV. Discussion

The focus of the underlying study was to investigate key statements related to the contrast enhancement of susceptibility maps in TE-dependent QSM in the healthy subject, algorithm performance evaluation in both patients, and in the case of the glioblastoma subject the use of multi-echo QSM, and the proposal of a superposed QSM method.

The investigations of Statement H 1 revealed that susceptibility map contrast enhances with increasing echo times. Researchers found out that setting the echo time to the average T2* of gray and white matter results in maximum phase contrast between them [12, 13]. Thus, the sixth echo ($TE_6 = 29.51\,ms$) provided the highest contrast for all algorithms. Sood et al. [14] conducted a study of regional dependence of susceptibility maps on echo time. The authors reconstructed GRE phase images ($TE_1 = 2.04\,ms$, 30 echoes, $\Delta TE = 1.53\,ms$) for five healthy volunteers at 7 T and found that mean susceptibility values decreased in the putamen and pallidum over time, while the caudate showed an initial increase followed by a decrease. Compared with this, the underlying results reveal a different behavior, as depicted in the graphs of Figure 4.

The mean susceptibility values at $TE_3 = 14.7\,ms$ echo time in the defined ROI from Table II can be compared to mean values calculated in the study of Sood et al. [14] at $TE = 15.81\,ms$. They mapped susceptibility values in the caudate ($0.040 \pm 0.015\,ppm$), putamen ($0.025 \pm 0.025\,ppm$), and pallidum ($0.079 \pm 0.015\,ppm$). These results show the highest correlation with the values reconstructed by the STAR-QSM algorithm, although they still differ. The variations can be attributed to differences in data acquisition procedures, reconstruction method, definition and segmentation of ROI, selection of reference tissue, subject attributes, and echo time choice.

However, high concentrations of iron are known to occur in brain regions such as the putamen and pallidum, whereas the caudate show a minor accumulation of iron [15, 16] which is best reflected with the RTS algorithm.

To evaluate the algorithm performance on a healthy dataset (Statement H 2), quantitative error metrics were computed for MEDI and RTS, with STAR-QSM chosen as the reference due to comparable susceptibility values found in literature [17]. RTS outperformed MEDI in terms of agreement (RMSE and HFEN) with the reference, while MEDI showed greater structural similarity (SSIM) to STAR-QSM. Generally, lower echo times produced better results across all metrics, except the second echo. As the echo time increases, agreement, and similarity decrease in both algorithms.

The graphs in Figure 5 are very similar for the first two metrics but with a clear offset. This offset may be attributed to the differences in susceptibility values, which differed more between MEDI and STAR-QSM than between RTS and STAR-QSM. Additionally, the high percentages in RMSE and HFEN may also be caused by the erroneous susceptibility values reconstructed by MEDI and RTS.

In the "2016 Reconstruction Challenge" [5] the performance of susceptibility maps from 27 algorithms was evaluated, including MEDI and RTS. The algorithms were compared to a Susceptibility Tensor Imaging (STI) algorithm that reconstructed susceptibility values of healthy patient data acquired from 12 head orientations. RTS outperformed MEDI in terms of RMSE (69%) and HFEN (68.9%), while MEDI scored higher in SSIM (0.93). These results correspond to the finding of the underlying study, even if the values differ significantly. However, it is worth noting that the participants in the challenge optimized their algorithms by tuning regularization parameters. Whereas in this study, all algorithms were run without changing any regularization parameters, most probably resulting in erroneous high and low susceptibility values for MEDI and RTS. Moreover, using STAR-QSM as a reference requires critical consideration, as artifacts in STAR-QSM itself could influence the results. One way to better evaluate the performance of the algorithms would be to refer to a gold standard technique, such as the one used in the reconstruction challenge or the Calculation Of Susceptibility through Multiple Orientation Sampling (COSMOS) method. Furthermore, Langkammer et al. [4] pointed out that the RMSE is usually an inadequate measure for assessing visual quality when over-smoothing through higher regularization constraints appears. This problem can be observed in the results of RTS as well. Although it revealed a better RMSE compared to MEDI, it resulted in an overly-smoothed reconstructed susceptibility map.

To overcome the limitations of relying solely on three fidelity metrics, an expert visual rating could provide a more comprehensive performance assessment, as demonstrated in the "Reconstruction Challenge 2.0" [18]. In addition, using an open-source algorithm that does not require adjustment of the regularization parameters across applications and datasets could reduce the problem of introducing erroneous susceptibility values. This could be adventurous, especially for inex-

perienced users and clinical applications. Stewart et al. [19] developed a QSM framework, QSMxT, with a straightforward implementation, resulting in robust results across all datasets by using default parameters.

The QSM results for the healthy patient showed only minor differences in reconstruction, particularly in terms of artifact generation. However, the performance of the algorithms for the glioblastoma patient varied significantly. This can be attributed to the fact that present QSM algorithms perform well in reconstructing healthy subject data, but QSM across high dynamic ranges of susceptibility values still remains challenging [19]. If no sufficient regularization is implemented, the unreliable phase introduces streaking artifacts on the final susceptibility map. Although the STAR-QSM algorithm attempted to address this issue by reducing streaking artifact propagation through specific steps, artifacts still appear in the susceptibility map. Next to the STAR-QSM algorithm, other recent techniques address this problem as well [19]–[21] by adapting the processing steps of QSM differently.

TE-dependent QSM measurements were performed, in order to investigate the algorithm performance using different masks on the tumor patient (Statement G 3). More precisely, the first masks were generated from the individual magnitude images of the varying echo times of the GRE sequence using FSL BET. The higher the echo time, the smaller the created mask. With increasing echo time, regions with rapid signal dropout are removed, resulting in an exclusion of the tumor region for the last echo brain mask. The individual masks, the E6 mask from the sixth echo only, and the T1 mask from the T1 weighted magnitude image were applied to the three different algorithms. The results showed that using the E6 mask led to overall good susceptibility map reconstructions in all algorithms, with the STAR-QSM algorithm performing best compared to MEDI and RTS. When other masks were applied, each algorithm exhibited artifacts like shadowing, streaking artifacts, and over-smoothing. The metric evaluation further reinforces this conclusion, with the severe streaking artifacts in RTS using the T1 mask being especially apparent in the course of each metric graph.

Although neglected in most of the QSM literature, signal masking to identify reliable phase signal regions for background field removal and dipole inversion is a crucial step [19] and influences the final susceptibility map, as demonstrated in the underlying results. Applying a smaller mask can reduce artifacts at the periphery of the ROI, but also comes with the risk that valuable phase data is rejected from the reconstruction. Excluding unreliable phase shifts, caused by pathological conditions for example, from reconstruction can be problematic in clinical settings when information about that tissue structure is of interest.

Recent deep learning-based QSM approaches showed good-quality susceptibility maps without the error-prone brain masking step [22, 23], which might be adventurous for clinical applications. Nevertheless, additional research and validation are necessary to evaluate the suitability of these methods [24].

To investigate Statement G 4, multi-echo QSM was performed using MEDI and STAR-QSM with the E6 and T1 masks and compared to TE-dependent measurements from before. The evaluations showed that the susceptibility maps produced with multi-echo STAR-QSM and the E6 mask showed the fewest artifacts.

Biondetti et al. [25] studied the accuracy and precision of multi-echo versus TE-dependent QSM using Laplacian-based methods for phase unwrapping and background field removal. Their research, involving 10 healthy volunteers on a 3 T scanner, revealed that multi-echo QSM resulted in higher regional accuracy in comparison to TE-dependent QSM, particularly at shorter TEs and in high-susceptibility regions. Generally, TE-dependent QSM can reveal intrinsic tissue property information [14] and benefits from noise reduction at longer TE values, while multi-echo QSM can provide TE-independent field maps with optimized SNR and reduced phase noise propagation in background field removal [25]. Multi-echo QSM with a larger number of combined echoes showed even less phase noise propagation into the final susceptibility map [26].

As STAR-QSM algorithms in multi-echo QSM showed the least artifact-prone reconstructed maps and susceptibilities closest to literature values, further statements were investigated using this method.

To investigate Statement G 5, a separate QSM calculation process for healthy and tumor-affected brain tissue was proposed to prevent phase errors from high-frequency shifts in the tumor region propagating into dominant QSM artifacts. The brain mask of the sixth echo was inverted to obtain the tumor mask. QSM calculations were performed on both masks with STAR-QSM, resulting in two individual susceptibility maps. One map contained susceptibility values without most of the tumor contribution, and the other map displayed only susceptibility values in the tumor region. Combining the two susceptibility maps yielded a superposed, whole-brain susceptibility map, outperforming regular full-brain mask reconstruction methods. In a similar study, Sun et al. [21] investigated a superposed dipole inversion method for QSM in intracranial hemorrhage (ICH). Their optimized reconstruction scheme combined a mask-inversion process with ICH isolation and subsequent superposition reconstruction, resulting in high-quality QSM images from eight ICH subjects. In comparison to this study, the authors generated the non-ICH brain mask after air/tissue background field removal by setting a threshold on the reconstructed QSM image and performed a second background field removal of air/tissue background and ICH dipole field. This represents an automated segmentation algorithm by adding an extra term to the regularization in the dipole inversion step, to mask out the corrupted phase introduced by the ICH. The results of the underlying study showed that the QSM merging method reduces artifacts compared to the mask merging method, but high susceptibility shifts still occur at the edge of the tumor, that were not properly masked using FSL BET. To enhance the minimization of artifact propagation to the final susceptibility map, precise masking of the tumor region by manual segmentation may lead to more sophisticated results. Most QSM techniques employ morphological erosion on input masks to improve background field removal and dipole inversion accuracy. Therefore, the tumor mask had to be dilated before applying it to the QSM pipeline. This dilation could create holes in the superposed whole-brain image when

merging the resulting QSM images. Further dilation, however, could lead to an overlap of both results, expanding the excluded brain mask region.

Nevertheless, the proposed method for a separate QSM calculation of the healthy and tumor-affected brain tissue outperformed any other method applied in this study, resulting in susceptibility maps with reduced streaking artifacts.

V. Conclusion

The present study showed that the propagation of streaking artifacts can be reduced by incorporating multi-echo QSM and excluding regions with high susceptibility shifts during reconstruction. Subsequent superposition of the missing susceptibility information composes of a full-brain susceptibility map with high quality and reduced artifacts. However, for any further examination and application, it is crucial to conduct investigations based on a larger cohort of patients. An expanded sample size will enable a more comprehensive evaluation of the proposed methods, allowing for precise determination of their accuracy, reproducibility, and reliability.

References

[1] C. Liu, W. Li, K. A. Tong, K. W. Yeom, and S. Kuzminski, "Susceptibility-weighted imaging and quantitative susceptibility mapping in the brain," *Journal of magnetic resonance imaging : JMRI*, vol. 42, no. 1, pp. 23–41, 2015. [Online]. Available: https://doi.org/10.1002/jmri.24768

[2] A. Deistung *et al.*, "Quantitative susceptibility mapping differentiates between blood depositions and calcifications in patients with glioblastoma," *PLOS ONE*, vol. 8, no. 3, p. e57924, 2013. [Online]. Available: https://doi.org/10.1371/journal.pone.0057924

[3] S. Zeng *et al.*, "Quantitative susceptibility mapping evaluation of glioma," *European radiology*, 2023. [Online]. Available: https://doi.org/10.1007/s00330-023-09647-4

[4] T. P. Reith *et al.*, "Basal Ganglia Iron Content Increases with Glioma Severity Using Quantitative Susceptibility Mapping: A Potential Biomarker of Tumor Severity," *Tomography (Ann Arbor, Mich.)*, vol. 8, no. 2, pp. 789–797, 2022. [Online]. Available: https://doi.org/10.3390/tomography8020065

[5] C. Langkammer *et al.*, "Quantitative susceptibility mapping: Report from the 2016 reconstruction challenge," *Magnetic resonance in medicine*, vol. 79, no. 3, pp. 1661–1673, 2018. [Online]. Available: https://doi.org/10.1002/mrm.26830

[6] M. Jenkinson, C. F. Beckmann, T. E. J. Behrens, M. W. Woolrich, and S. M. Smith, "FSL," *NeuroImage*, vol. 62, no. 2, pp. 782–790, 2012. [Online]. Available: https://doi.org/10.1016/j.neuroimage.2011.09.015

[7] P. A. Yushkevich *et al.*, "User-guided 3D active contour segmentation of anatomical structures: significantly improved efficiency and reliability," *NeuroImage*, vol. 31, no. 3, pp. 1116–1128, 2006. [Online]. Available: https://doi.org/10.1016/j.neuroimage.2006.01.015

[8] E. Biondetti *et al.*, "Multi-echo quantitative susceptibility mapping: how to combine echoes for accuracy and precision at 3 Tesla," *Magnetic resonance in medicine*, vol. 88, no. 5, pp. 2101–2116, 2022. [Online]. Available: https://doi.org/10.1002/mrm.29365

[9] A. Deistung, F. Schweser, and J. R. Reichenbach, "Overview of quantitative susceptibility mapping," *NMR in biomedicine*, vol. 30, no. 4, 2017. [Online]. Available: https://doi.org/10.1002/nbm.3569

[10] S. Ravishankar and Y. Bresler, "MR image reconstruction from highly undersampled k-space data by dictionary learning," *IEEE transactions on medical imaging*, vol. 30, no. 5, pp. 1028–1041, 2011. [Online]. Available: https://doi.org/10.1109/TMI.2010.2090538

[11] Z. Wang, A. C. Bovik, H. R. Sheikh, and E. P. Simoncelli, "Image quality assessment: from error visibility to structural similarity," *IEEE transactions on image processing : a publication of the IEEE Signal Processing Society*, vol. 13, no. 4, pp. 600–612, 2004. [Online]. Available: https://doi.org/10.1109/tip.2003.819861

[12] S. C. Chu, Y. Xu, J. A. Balschi, and C. S. Springer, "Bulk magnetic susceptibility shifts in NMR studies of compartmentalized samples: use of paramagnetic reagents," *Magnetic resonance in medicine*, vol. 13, no. 2, pp. 239–262, 1990. [Online]. Available: https://doi.org/10.1002/mrm.1910130207

[13] J. H. Duyn *et al.*, "High-field MRI of brain cortical substructure based on signal phase," *Proceedings of the National Academy of Sciences of the United States of America*, vol. 104, no. 28, pp. 11 796–11 801, 2007. [Online]. Available: https://doi.org/10.1073/pnas.0610821104

[14] S. Sood *et al.*, "Echo time-dependent quantitative susceptibility mapping contains information on tissue properties," *Magnetic resonance in medicine*, vol. 77, no. 5, pp. 1946–1958, 2017. [Online]. Available: https://doi.org/10.1002/mrm.26281

[15] B. Drayer *et al.*, "MRI of brain iron," *AJR. American journal of roentgenology*, vol. 147, no. 1, pp. 103–110, 1986. [Online]. Available: https://doi.org/10.2214/ajr.147.1.103

[16] E. M. Haacke *et al.*, "Imaging iron stores in the brain using magnetic resonance imaging," *Magnetic resonance imaging*, vol. 23, no. 1, pp. 1–25, 2005. [Online]. Available: https://doi.org/10.1016/j.mri.2004.10.001

[17] H. Wei *et al.*, "Streaking artifact reduction for quantitative susceptibility mapping of sources with large dynamic range," *NMR in biomedicine*, vol. 28, no. 10, pp. 1294–1303, 2015. [Online]. Available: https://doi.org/10.1002/nbm.3383

[18] B. Bilgic *et al.*, "QSM reconstruction challenge 2.0: Design and report of results," *Magnetic resonance in medicine*, vol. 86, no. 3, pp. 1241–1255, 2021. [Online]. Available: https://doi.org/10.1002/mrm.28754

[19] A. W. Stewart *et al.*, "QSMxT: Robust masking and artifact reduction for quantitative susceptibility mapping," *Magnetic resonance in medicine*, vol. 87, no. 3, pp. 1289–1300, 2022. [Online]. Available: https://doi.org/10.1002/mrm.29048

[20] N. Yaghmaie *et al.*, "QSMART: Quantitative susceptibility mapping artifact reduction technique," *NeuroImage*, vol. 231, p. 117701, 2021. [Online]. Available: https://doi.org/10.1016/j.neuroimage.2020.117701

[21] H. Sun *et al.*, "Quantitative susceptibility mapping using a superposed dipole inversion method: Application to intracranial hemorrhage," *Magnetic resonance in medicine*, vol. 76, no. 3, pp. 781–791, 2016. [Online]. Available: https://doi.org/10.1002/mrm.25919

[22] W. Jung, S. Bollmann, and J. Lee, "Overview of quantitative susceptibility mapping using deep learning: Current status, challenges and opportunities," *NMR in biomedicine*, vol. 35, no. 4, p. e4292, 2022. [Online]. Available: https://doi.org/10.1002/nbm.4292

[23] S. Bollmann *et al.*, "SHARQnet - Sophisticated harmonic artifact reduction in quantitative susceptibility mapping using a deep convolutional neural network," *Zeitschrift fur medizinische Physik*, vol. 29, no. 2, pp. 139–149, 2019. [Online]. Available: https://doi.org/10.1016/j.zemedi.2019.01.001

[24] B. Bilgic *et al.*, "Recommended Implementation of Quantitative Susceptibility Mapping for Clinical Research in The Brain: A Consensus of the ISMRM Electro-Magnetic Tissue Properties Study Group," *ArXiv*, 2023. [Online]. Available: https://pubmed.ncbi.nlm.nih.gov/37461418/

[25] E. Biondetti, A. Karsa, D. L. Thomas, and K. Shmueli, "Investigating the accuracy and precision of TE-dependent versus multi-echo QSM using Laplacian-based methods at 3 T," *Magnetic resonance in medicine*, vol. 84, no. 6, pp. 3040–3053, 2020. [Online]. Available: https://doi.org/10.1002/mrm.28331

[26] T. Liu *et al.*, "Cerebral microbleeds: burden assessment by using quantitative susceptibility mapping," *Radiology*, vol. 262, no. 1, pp. 269–278, 2012. [Online]. Available: https://doi.org/10.1148/radiol.11110251